Erschienen in: Advanced Functional Materials ; 27 (2017), 7. - 1604532
https://doi.org/10.1002/adfm.201604532

Toroidal Protein Adaptor Assembles Ferrimagnetic Nanoparticle Fibers with Constructive Magnetic Coupling

Tuan Anh Pham, Andreas Schreiber, Stefan M. Schiller, and Helmut Cölfen**

Inspired by nature, the synthesis of biohybrid nanocomposites containing inorganic nanoparticles (NPs) and biopolymers such as DNA and peptides as templates offers great potential for a wide range of applications. Using selective recognition schemes of 3D protein spaces for the assembly of magnetic nanocrystals is a challenge with great promise in the field of biomedicine and magnetic data storage. Here we apply the toroidal protein Hcp1 as an interparticle connector for the directed molecular assembly and ferrimagnetic coupling of biohybrid cobalt ferrite NP wires. The resulting biohybrid NP composites show bundles of nanofibers ranging from nano- to the microscale in length verified by TEM, EDX analysis and focused ion beam cut. Their magnetic characterization reveals an increase of the coercive field (+12%) reaching values of high-end $Nd_2Fe_{14}B$ bulk magnets, enhanced saturation (+28%) and remanence magnetization (+38%) at 2 K compared to NPs lacking the protein connector. Thus, the combination of the nanoscale alignment of magnetic NPs with the molecular precision of the protein connectors leads to constructive addition of the magnetization reversal energy. This approach can be used to control magnetic properties for the design of materials with enhanced coercivity applicable for magnetic data storage, hyperthermia and theranostics.

1. Introduction

Hybrid magnetic nanocomposite materials are of technological interest because multiple properties and useful functions can be combined within a single material. Hence, composite materials show tailorable properties that improve beyond those of the individual components. A major scientific interest is the control of magnetic properties for use in various practical applications ranging from high-density data storage devices[1] and high-performance nanocomposite bulk magnets[2] to theranostics.[3] Theranostics, which describes a combination of diagnostic and therapeutic function is very promising for the treatment of various human cancers[4–6] by combining magnetic resonance imaging (MRI) and magnetic hyperthermia treatment (MHT).[7]

For the production of patterned magnetic assemblies, usually classical top down lithographic- and nanoimprint techniques have been applied.[1,8] However, there is an increasing number of developments in template-based methods for the preparation and processing of magnetic nanoparticles (MNPs). Therefore inorganic templates such as: SiO_2[9–11] and aluminum oxide;[12] and also organic polymers;[13–15] have been employed as matrices for the fabrication of NP array structures and high-density data storage materials. However, nature offers attractive biomineralization methods that allow for the direct synthesis and assembly of crystalline inorganic materials under environmentally benign conditions. In many organisms, biomolecules such as: DNA,[16] peptides,[17] proteins,[18] and polysaccharides[19] play a critical role in the biomineralization process. A prominent example are magnetotactic bacteria which contain nano-sized, membrane bound magnetic iron oxide crystals called magnetosomes, organized into chains.[20,21] This enables the bacteria to use the magnetite chain as a very sensitive sensor for the geomagnetic field. Bottom up manufacturing, using biological molecules that template magnetic materials, includes several advantages over conventional lithographic methods. These advantages are due to 3D molecular protein spaces with well-defined recognition motifs, which allow for the cost efficient precise organization of magnetic material at room temperature. Inspired by nature, biomolecules such as porous protein crystals,[22] protein cages,[23] cellulose nanostructures,[24,25] and DNA[26] have been used for the patterning of MNPs. Moreover patchy protein structures have been applied to trigger γ–Fe_2O_3 NP assembly into binary superlattice or array structures[27,28] and peptides have been used as biotemplates for the 1D assembly of magnetic NPs into nanowires.[29] When MNPs are incorporated into matrices, particle alignment and spatial confinement result in enhanced magnetic characteristics such as saturation magnetization (M_s), remanence magnetization (M_R), coercivity (H_C), and blocking temperature (T_b). However, often the low compatibility of the NPs with the matrices causes an inhomogeneous distribution of the

Dr. T. A. Pham, Prof. H. Cölfen
Department of Chemistry
Physical Chemistry
University of Konstanz
Universitätstrasse 10, D-78457 Konstanz, Germany
E-mail: helmut.coelfen@uni-konstanz.de
Dr. A. Schreiber, Dr. S. M. Schiller
Zentrum für Biosystemanalyse (ZBSA)
Albert-Ludwigs-Universität Freiburg
Habsburgerstrasse 49, D-79104 Freiburg, Germany
E-mail: stefan.schiller@frias.uni-freiburg.de

inorganic component within the nanocomposite. Therefore, a more sophisticated approach, such as matrix-free assembly, is needed to create regularly organized nano-objects. In the protein-adaptor-based-nano-object-assembly (PABNOA) concept Schreiber and co-wokers[30] used the molecularly confined Hcp1 protein structure as an adaptor to connect NPs forming biohybrid nanocomposites with 1D structure. This approach has been previously used for the assembly of CdSe-, Au-, and magnetite NPs.[30–32] Extending the utility of the PABNOA approach, here we show the matrix-free assembly of magnetically coupled cobalt ferrite ($CoFe_2O_4$ NP) nanofibers. Following the principle from structure to function, we yield nanocomposite fibers, from the nano- to the microscale in length, with enhanced magnetic properties when compared with unassembled NPs reaching those of the strongest Nd bulk magnets. To enhance the effects, that nanoscale alignment has on the magnetization of ferrite NPs,[30] $CoFe_2O_4$,[33] which has a high coercivity when compared to magnetite, has been used in this work. The resulting Hcp1-$CoFe_2O_4$ nanocomposite material exhibits increased H_C, M_S, and M_R compared to the nonprotein containing MNPs, as analyzed with superconducting quantum interference device (SQUID) measurements. Bundles of nanofibers microns in the length are revealed by scanning electron microscopy (SEM) and transmission electron microscopy (TEM). Extensive characterization of the $CoFe_2O_4$ NP components was conducted via infra red (IR), X-ray diffraction (XRD), and energy electron loss spectroscopy (EELS). High-resolution TEM (HRTEM) images and energy dispersive X-ray (EDX) analysis demonstrates the stacking of $CoFe_2O_4$ NPs into chains inside the composite protein fibers. Focused ion beam (FIB) cut investigations show that the $CoFe_2O_4$ NPs are homogenously distributed within the fibers. Hence, the bottom up self-assembly using the 3D molecularly defined Hcp1 protein structure allows for the fabrication of biohybrid fibers with increased magnetic properties in H_C, M_S, and M_R.

2. Results

2.1. Nanofiber Building Blocks

The main component of the protein-driven self-assembly method used here is the 3D molecularly defined Hcp1 protein. As described elsewhere,[34] Hcp1 is a toroidal homohexameric protein structure with an outer diameter of 9.0 nm, an inner cavity diameter of 4.0 nm, and a height of 4.4 nm (Figure S1, Supporting Information). Through molecular cloning techniques, interaction motifs were implemented at strategic points on the Hcp1 upper, lower, and inner ringside of the protein surface (**Figure 1**I-A–C). Yielding a total of three solvent accessible cysteine residues per monomer, the bisfunctional Hcp1_cys3 mutant provides strong and directional binding affinity for different metallic NPs. Our previous works demonstrate that the cysteines of Hcp1_cys3 to bind Au-, CdSe-, and magnetite NPs.[30–32] From these observations, strong binding to $CoFe_2O_4$ NPs can be assumed as well

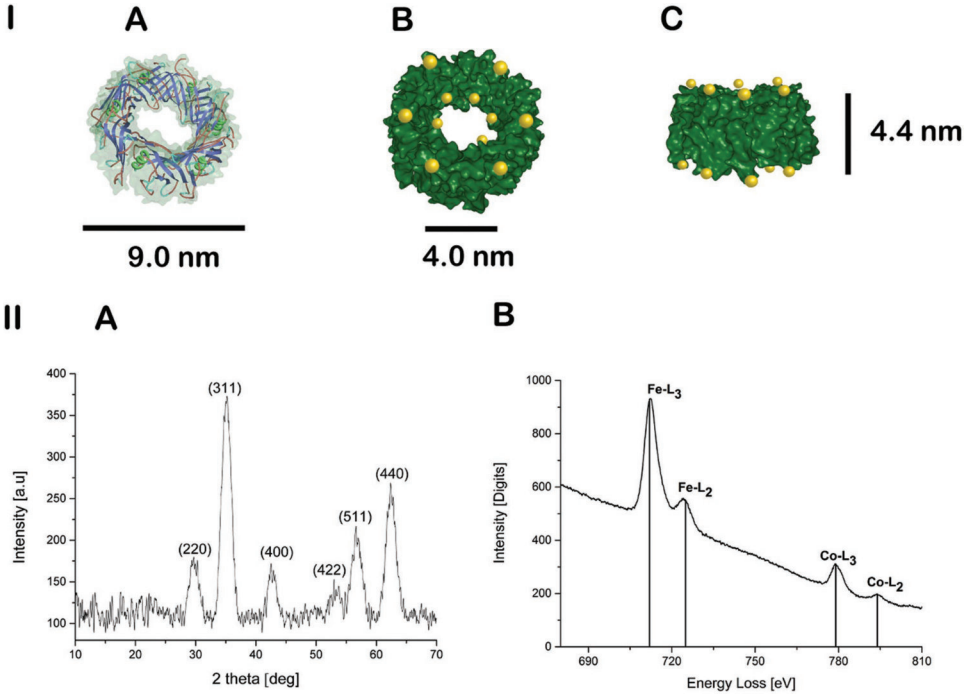

Figure 1. Building block characterization. I) Conformational and surface structure of Hcp1_cys3 [PDB, code: 1Y12]. I-A) Secondary structure elements of Hcp1 (beta sheet in blue, alpha helix in green, coil in red and turn in light blue). I-B,C) Surface of Hcp1_cys3 in side and top view, and the yellow spots indicate the six cysteine groups on the top, bottom, and inner cavity of the protein ring, which provide the binding sites for the NPs. The Hcp1 cavity spans an inner diameter of 4 nm, an outer diameter of 9 nm, and a height of 4.4 nm. II) Structural characterization by XRD and EELS show the successful synthesis of the aimed cobalt ferrite NPs. II-A) The XRD data confirms the spinel ferrite structure of the desired NPs and II-B) the EELS spectrum reveals the match of the cobalt and iron bands of our sample with the database (black lines) provided by the TEM software iTEM.

(Figure 1I-A–C). In order to yield a valuable nanocomposite material with high coercivity, the inorganic NP component ($CoFe_2O_4$ NP) with high-magnetocrystalline anisotropy was used.

The cobalt ferrite NPs ($CoFe_2O_4$ NPs) were synthesized by the protocol of Cabrera et al. (for details see the Methods section in the Supporting Information).[35] The synthesis yielded oleic acid stabilized NPs with a mean size of 5.5 ± 0.8 nm (see TEM image in Figure S2A in the Supporting Information). Structural characterization by XRD and EELS indicates the successful synthesis of cobalt ferrite as desired (Figure 1II-A,B). The XRD diffraction patterns can be assigned to the spinel structure of ferrite[35] and EELS analysis clearly confirmed the presence of cobalt in the NPs. The ratio between Co and Fe atoms was calculated to be closely 1:2 as measured via quantitative EDX analysis, which matches the Co:Fe ratio of 1:2 in $CoFe_2O_4$ material (Data S1, Supporting Information). In order to render the $CoFe_2O_4$ NPs water soluble and suitable for a protein aqueous environment, a ligand exchange against phosphonoacetic acid (PsAA) was conducted following the protocol of Lees et al.[36] After ligand exchange the size of the NPs remained at 5.5 ± 0.8 nm as shown in TEM. Successful exchange of oleic acid for PsAA was confirmed by the attenuated total reflection-infrared spectroscopy (ATR-IR), where characteristic IR bands of PsAA were seen after exchange (Figure S2B–D, Supporting Information).

2.2. Biohybrid Nanofiber Assembly

For the fabrication of the nanocomposite, the water soluble $CoFe_2O_4$ NPs were aligned in an external magnetic field and Hcp1_cys3 protein was added slowly. Following overnight incubation, the mixture was lyophilized and SEM characterization of the nanocomposite material reveals an extended fiber bundle structure of 20–80 μm in length and 1–2 μm in width as determined from SEM images (**Figure 2**I-A,B). TEM images of the nanocomposite deposited on the TEM grid during assembly reveals individual NP chains within the fiber structure of the bundles observed in SEM (Figure 2I-C). At higher magnification nanofiber-like structures of NP chains are visible (Figure 2I-B,C). During drying the interaction between the TEM grid and the NP chains leads to a more open structure compared to samples lyophilized and assembled from solution without a TEM grid, visible in SEM images (Figure 2I-A,B). The width of a single NP chain, composed of a $CoFe_2O_4$ core and the surrounding organic layer, matches the diameter of the Hcp1_cys3 protein structure (9 nm) as shown on the HRTEM image in Figure 2I-D. This indicates that Hcp1_cys3 is located in-between two adjacent NPs with nearly complete penetration into the protein cavity (Figure 2I-E). An interparticle distance of 0.8 ± 0.3 nm in the HRTEM image can be determined (Data S2, Supporting Information), which is less than the 2.67 nm distance calculated based on the protein crystal structure.[30] This result indicates a flexible Hcp1 ring structure, which results in

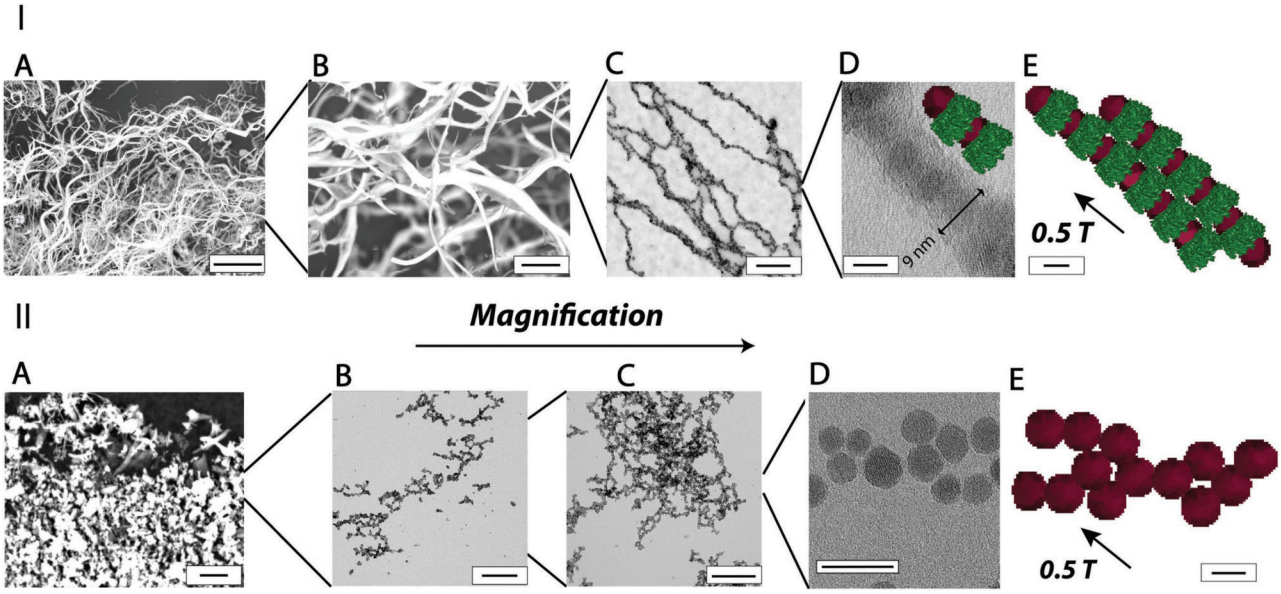

Figure 2. SEM and TEM images of $CoFe_2O_4$ NPs assembled in a magnetic field to I) biohybrid fibers in the presence of Hcp1_cys3 and to II) nonspecific NP agglomerates in the absence of the protein connector. I-A,B) SEM images of $CoFe_2O_4$–Hcp1_cys3 fibers after lyophilization. I-C,D) TEM images of $CoFe_2O_4$–Hcp1_cys3 sample reveal linear alignment of the NPs on the μm and nm scales after lyophilization on the TEM grid. I-D) HRTEM image of a single $CoFe_2O_4$ NP in a chain reveals crystalline $CoFe_2O_4$ core surrounded by an organic layer of a diameter of 9 nm, which matches the outer diameter of Hcp1_cys3 indicating that the NPs are almost completely trapped inside the protein cavity. I-E) Schematic illustration of the molecular assembly. II-A) SEM image of $CoFe_2O_4$_Ref control sample reveals nonspecific agglomerates. I-A,B) The control sample was prepared by the same protocol as above, but without Hcp1_cys3 protein addition. II-B–D) TEM images of $CoFe_2O_4$_Ref show the randomly oriented cobalt ferrite NPs. II-D) HRTEM image of a single $CoFe_2O_4$ NP chain without the surrounding organic layer of Hcp1_cys3. II-E) Schematic illustration of the molecular assembly. Images are ordered from left to right with increasing magnification and scale bars represent I-A) 50 μm, I-B) 10 μm, I-C) 200 nm, I-D) 5 nm, I-E) 5 nm, II-A) 5 μm, II-B) 200 nm, II-C) 200 nm, II-D) 10 nm, II-E) 5 nm.

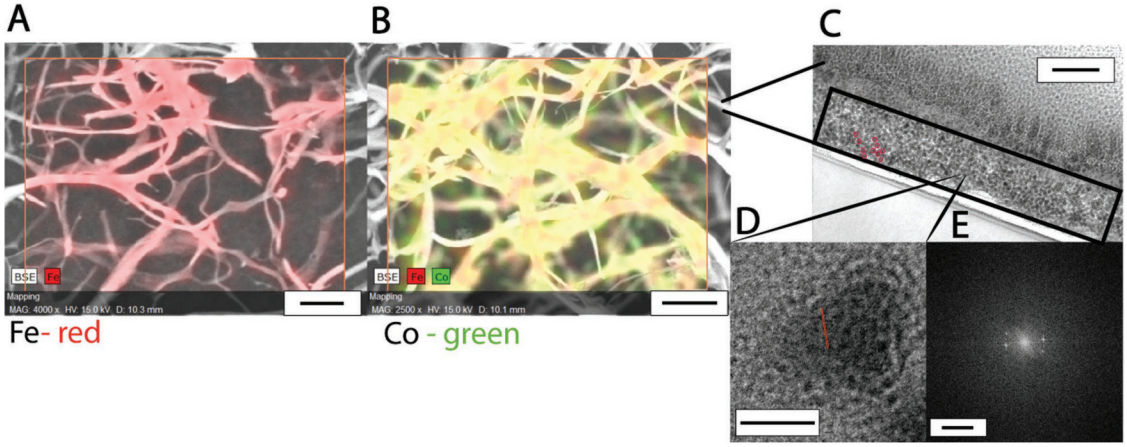

Figure 3. EDX analysis of $CoFe_2O_4$–Hcp1_cys3 fiber structure on the µm scale shows iron (red) and cobalt (green) presence in these fibers (red and green results in the yellow color). C) TEM image of a FIB cut along the long axis of the nanocomposite fiber (black square) shows a layer of cobalt ferrite NPs (red circles) with a height of 100 nm and length of 400 nm. The upper and lower parts are deposited silicon oxide layer for stabilization and the silicon substrate. D) HRTEM image of the FIB cut shows single NP with a distance between the lattices (red line) of about 2.9 Å matching the (2,2,0) face cobalt ferrite bulk material. E) The FFT diffraction can also be assigned to the (2,2,0) face of a cobalt ferrite material. Scale bars represent A) 5 µm, B) 10 µm, C) 100 nm, D) 5 nm, E) 5 1/nm.

a greater penetration depth of the NP into the protein cavity leading to a smaller interparticle distance. Another reason for this smaller distance could be due to the drying process on the TEM grid, since a dried protein is much smaller than in its hydrated crystal structure. Furthermore, the surface contacts between the particles and the protein, and magnetic attraction between the particles, may also lead to contraction and compression of the protein parts of the fibers. Based on the detected signals for iron and cobalt, the EDX analysis evidences a homogeneous distribution of the NPs in these fibers (**Figure 3**A,B). Additionally, a ratio between Co and Fe was determined to be ≈1:2 by quantitative EDX analysis, matching the Co:Fe ratio of the NPs (Data S1, Supporting Information). A TEM image of a FIB section along the length of a $CoFe_2O_4$ NP containing fiber (Figure 3C) shows the stacking of NPs in the center of the cut with a height of 100 nm and a length of 400 nm. The HRTEM and fast-Fourier-transform (FFT) images in Figure 3D,E confirm that the observed nanostructure with a lattice distance of 2.897 Å is the (2,2,0) face of cobalt ferrite.[37] The FIB cut result supports the SEM and TEM data showing homogeneous distributed cobalt ferrite NP inside the protein-based fibers.

In order to demonstrate the importance of the protein adaptor Hcp1 for the fiber assembly, a reference sample ($CoFe_2O_4$_Ref) was prepared as control. Applying the same assembly method as described above but lacking the Hcp1_cys3 protein addition gave spherical NP agglomerates in the SEM (3 ± 1.5 µm in size) and randomly aligned cobalt ferrite NPs in the TEM images, lacking the organic Hcp1 layer (Figure 2II-A–D). This reference experiment verified important effects of our concept for utilizing Hcp1_cys3 as a protein adaptor for enhanced fiber-like $CoFe_2O_4$ nanocomposite assembly. A strong interaction between cysteine side chains and ferrite surfaces, which was also reported by Cohen et al.,[38] is responsible for Hcp1_cys3–$CoFe_2O_4$ NPs alignment. However, the abundance of carboxyl groups on the Hcp1 rim sides (see Figure S1 in the Supporting Information and pdb 1y12)[34] might also contribute to the ferrite NP binding as demonstrated by Schwamminger et al.[39] In addition to the importance of the Hcp1_cys3 protein adaptor for controlled self-assembly, dipole–dipole interactions, as stated in Schreiber et al.,[32] play a crucial role as well. In previous studies,[32] Hcp1_cys3 guided gold nanoparticles (AuNPs) to assemble into different nanoarchitectures. The application of Hcp1wt control, lacking the additional thiol groups (Data S3, Supporting Information) did not lead to any Hcp1-AuNP assembly. Furthermore, in the presence of an external magnetic field, magnetic Hcp1_cys3 induced dipole–dipole interactions pivotal for the assembly of nanoparticles from liquid dispersions.[40]

2.3. Nanofiber Assembly Leads to Enhanced Ferrimagnetism

As the aim of this work was the design of magnetically coupled NP wires to yield a nanomaterial with increased coercivity, the resulting magnetic properties were investigated by SQUID measurements. As intended, the formation of the nanocomposite structure significantly enhances the M_S values at 300 and 2 K, as well as the M_R value of our cobalt ferrite NPs (**Figure 4**). In addition, physical connection via the Hcp1 protein adaptor leads to magnetic coupling of NPs and subsequently to an increase of the H_C value by 2200 Oe (+12.3%) compared to the reference sample ($CoFe_2O_4$ Ref) (Figure 4A,B). A summary of the magnetic data is listed in **Table 1**. These results can be explained by the Hcp1_cys3 induced structural anisotropy leading to constructive addition of the potentials for magnetization reversal of the $CoFe_2O_4$ NPs.[11] This corresponds well to the results of cobalt NPs where uniaxial coupling of NPs in 1D chains caused magnetizing effects, such as an increase in coercivity.[41] The obtained H_C value of 20 100 Oe of our Hcp1-$CoFe_2O_4$ hybrid fibers at 2 K (19 092 Oe at 5 K in **Figure 5**C) is approximately eightfold higher than the aligned CoNP of Gross et al. (H_C of 2450 Oe at 5 K).[11] A noncomprehensive list of reported H_C values at 5 K of comparable MNP assemblies can be found in Data S4 in the Supporting Information.

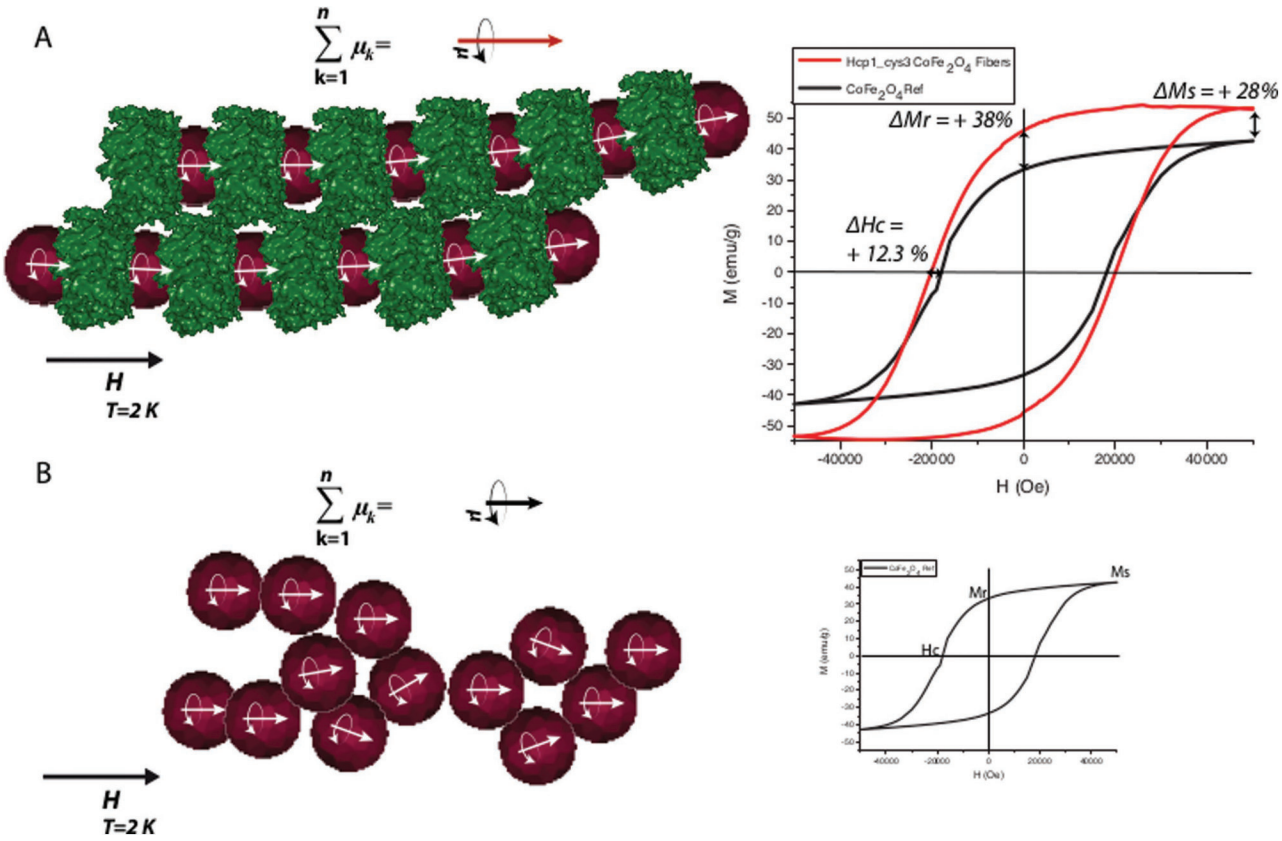

Figure 4. Hcp1_cys3 guided assembly of Hcp1_cys3–$CoFe_2O_4$ fibers leads to enhanced magnetic properties. A) 1D assembly and ferrimagnetic coupling of uniaxial Hcp1_cys3–$CoFe_2O_4$ fibers leads to constructive addition of magnetization reversal potential (μ) and increased H_C, M_R, and M_S at 2 K (red line). B) Interactions of agglomerated $CoFe_2O_4$ NPs lead to less constructive ferrimagnetic coupling and thus decreased H_C, M_R, and M_S of the control $CoFe_2O_4$ Ref (black line). *H*, magnetic field strength; μ, potential of magnetization reversal; *n*, number of particles.

Furthermore, the Hcp1_cys3–$CoFe_2O_4$ NPs alignment leads to an increased (+7.5%) M_R/M_S ratio (squareness of the hysteresis) when compared to the reference sample (Table 1). This can be explained by the stabilization of the Hcp1-$CoFe_2O_4$ hybrid fiber magnetization by dipolar interactions along the easy axis of the aligned fibers. These interactions originate from the shape anisotropy generated by the linear assembly of the coupled particles and are reported for Fe[42] and $Nd_2Fe_{14}B$[43] NP chains as well. This is supported by the higher (+44%) effective anisotropy constant (K_{eff}) of the Hcp1_cys3–$CoFe_2O_4$ hybrid fibers when compared to the $CoFe_2O_4$ Ref sample, which is similar to cobalt ferrite bulk material of 20×10^5 erg cm^{-3} (Table 1).[44,45] K_{eff} can be calculated as[46]

$$K_{eff} = M_S \times H_C/2 \quad (1)$$

and elevated K_{eff} values (see Table 1) of NPs originate from different size/shape distribution and ligand/solvent molecules on the NP surface leading to increased shape- and surface anisotropy when compared to the ideal bulk material.[47] Therefore, the increase in K_{eff} results from the Hcp1_cys3–$CoFe_2O_4$ NP surface interaction and NP alignment. For the zero field cooling (ZFC) measurement the magnetization was recorded during warming of the sample from 2 to 300 K in 1 K steps. The field cooling (FC) measurement was carried out by cooling at the same rate in the same applied field as used for the ZFC measurement. Despite the increased K_{eff}, there is no difference between the blocking temperature of Hcp1_cys3–$CoFe_2O_4$ fibers and $CoFe_2O_4$_Ref as depicted in the ZFC and FC curves (Table 1, Figure S4, Supporting Information).

Table 1. Magnetic properties M_S, M_R, M_R/M_S ratio, H_C, K_{eff}, and T_{max} in ZFC curve of $CoFe_2O_4$_Ref sample and Hcp1–$CoFe_2O_4$ fibers.

	Hcp1_cys3–$CoFe_2O_4$ fibers	$CoFe_2O_4$ Ref
M_S at 300 K [emu g^{-1}]	47.75	38.87
M_S at 2 K [emu g^{-1}]	53.51	41.53
M_R at 2 K [emu g^{-1}]	46.03	33.33
M_R/M_S	0.86	0.80
H_C at 2 K [Oe]	20 100	17 900
K_{eff} [$\times 10^5$ erg cm^{-3}]	28.50	19.75
T_{max} [K]	180	180

2.4. From Ferrimagnetic to Superparamagnetic Hcp1_cys3–$CoFe_2O_4$ Fibers

The magnetization of these single-domain cobalt ferrite NP fibers at room temperature is nearly zero (Figure S5, Supporting

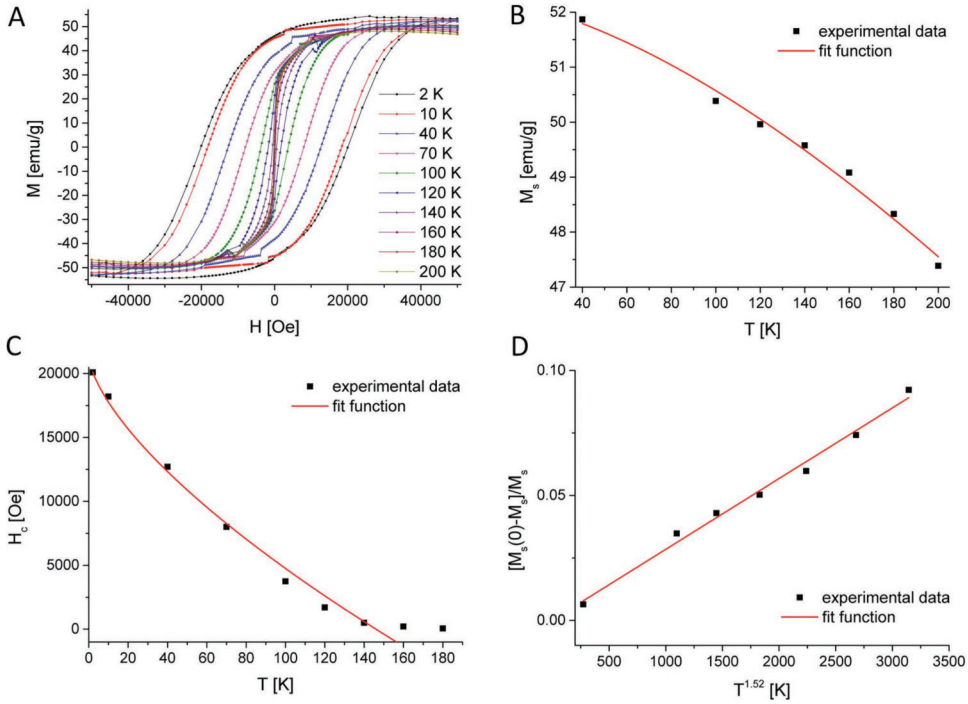

Figure 5. A) Hysteresis curves at different temperatures illustrate the transition from ferrimagnetic at low temperature to paramagnetic behavior above 160 K. B,C) The saturation magnetization (M_S) in (B) and coercivity (H_C) in (C) extracted from (A) decrease with increasing temperatures and can be plotted by the fit function (red line). D) The linear dependence of $M_S(0)-M_S(T)/M_S$ and $T^{1.52}$ verified the quality of the fit function in (B).

Information), rendering them superparamagnetic. The temperature dependency of the H_C values is demonstrated in Figure 5A and verifies the superparamagnetic nature of the Hcp1_cys3–$CoFe_2O_4$ fibers. Extracted M_S and H_C values from the hysteresis curves indicate decreasing H_C values with increasing temperatures (Figure 5B,C). This temperature dependent magnetization behavior reveals the transition from ferrimagnetism at low temperature to paramagnetism at high temperature. The thermal energy barrier needed for flipping can be described as T_b and is defined in Equation (S1) in the Supporting Information. Above T_b, the thermal energy is sufficient to enable free orientation of magnetic spins, and the Hcp1_cys3–$CoFe_2O_4$ fibers become superparamagnetic. Below T_b, the free rotation of spins is blocked by magnetocrystalline anisotropy. Thus, the volume dependency of the T_b and the applied NP size of 5.5 nm lead to a lacking hysteresis loop at 300 K (Figure S5A, Supporting Information) and the superparamagnetic behavior of our Hcp1-$CoFe_2O_4$ fibers.

In order to calculate the Bloch constant (B) and the Bloch exponent (α), M_S data were fitted by the Bloch law

$$M_S = M_S(0)\left[1 - BT^{\alpha}\right] \quad (2)$$

where $M_S(0)$ is the saturation magnetization at 0 K. The temperature dependent magnetizations of Hcp1_cys3–$CoFe_2O_4$ fibers (Figure 5B) reveal the following values: $B = 2.93 \times 10^{-5}$ $K^{-1.52}$, $\alpha = 1.52$, and $M_S(0) = 52.19$ emu g^{-1}. The obtained values match those reported in the literature well, since B is in the same order of magnitude as reported for Fe_3O_4[46] and $CoFe_2O_4$[25] NPs (3.3×10^{-5} K and 5.8×10^{-5} K), respectively. The Bloch exponent is slightly higher than the value characteristic to the bulk crystalline material and 3.3 nm $CoFe_2O_4$ NPs (α =1.5 for both).[48,49] Thus, our experimentally obtained α and B values are in agreement to reported values and small differences arise from various factors such as size, synthesis protocol, and surface stabilization.[50]

Fitting of the H_C values shown in Figure 5C by using Equation (S2) (Supporting Information) yields a coercive field at 0 K $H_C(O)$ = 21 343 Oe and a T_b of 154 K, which is in agreement with the T_b of cobalt ferrite NP of similar size.[51] Supporting the estimated T_b from the H_C-T fit function, the H_C values between 140 and 160 K only change slightly (Figure 5C). In addition the depicted fit function (Equation 4) in Figure 5D

$$M_{(S)}(0) - M_S(T) / M_S \text{ over } T^{1.52} \quad (3)$$

supports the quality of the M_S–T fit function (Figure 5B) since it follows a linear relation along the whole experimental temperature range and delivers an M_S–temperature relation with B and α, being consistent with published results for superparamagnetic NPs (Figure 5D).[46]

3. Conclusion

Molecular adaptor-based self-organization of nano-objects allows precise control of parameters such as the interparticle distances, and their local chemical and physical environment. Expanding the PABNOA approach from quantum dots[31] and AuNPs[32] assembly to the self-assembly of Hcp1_cys3–$CoFe_2O_4$ fibers leads to a new nanomaterial with enhanced magnetic properties reaching those of high-end Nd magnets[52] at 2 K

and linear NP structures. Well defined 3D molecular protein spaces with genetically implemented interaction points on the Hcp1_cys3 rim surface guide the 1D stacking of $CoFe_2O_4$ NPs chains. The final hybrid structures range from nano- to microscale in length and the EDX and FIB cut results show a homogeneous NP distribution inside the fibers. In this way, easy to synthesize isotropic NPs align into uniaxial NP chains resulting in anisotropic ferrimagnetic interparticle coupling. The constructive addition of demagnetization reversal potentials leads to an increase in H_C, M_S, and M_R at 2 K. As the sample was measured at low temperature, the influence of the thermal energy barrier on the hysteresis curve can be excluded and the actual barrier of magnetization reversal is directly extracted from the hysteresis width.[11] Thus, we conclude that magnetic anisotropic coupling of single NPs can be associated with an increase in K_{eff}, H_C, M_R, and M_S[11,41,53] which is greatly desired for the design of high-density data storage material. However, for the application of this approach for high-density data storage in the future, the magnetic fibers have to be surface attached and the T_b of the NPs needs to be increased above 300 K. The latter, can be achieved by using NPs of 10–12 nm in size showing increased H_C and T_b[54] for the assembly of Hcp1_cys3–$CoFe_2O_4$ NPs fibers. From such experiments, a higher T_b is expected since T_b increases proportionally with NP volume to about 370 K for CoNP at 13 nm[54] (for details see Equation (S1) in the Supporting Information). The required surface attachment and patterning of Hcp1_cys3–$CoFe_2O_4$ NPs fibers could be achieved by using surface functionalized nickellated nitrilotriacetic acid (NTA) binding the subunits of the Hcp1 histags.[55,56] Therefore, the selective attachment of Hcp1 organized magnetic nanoparticle chains to surfaces could provide a low temperature alternative to the current high-temperatures methods used to manufacture high-density data storage.[57]

In addition to the control over magnetic properties for applications in recording media,[58] our nanocomposite fiber material could also open the door for applications in nanomedicine,[54] magnetic hyperthermia,[6,59] and theranostics.[3] The dual character of the Hcp1 protein allows not only for binding to $CoFe_2O_4$ NPs but also for the fusion of epitopes, e.g., epidermal growth factor[60] or folate[61] and targeting of human tumor cells in vivo. After selective tumor cell binding of the epitope fused to Hcp1_cys3–$CoFe_2O_4$ NPs fibers, the exposure to an alternating magnetic field would induce heating and selective killing of cancer cells. In this context, a very promising study has shown that magnetosomes organized into chains very efficiently killed breast cancer cells in suspension and eradiated a xenographed tumor in mice upon exposure to an alternating magnetic field.[62] This and a subsequent study of Alphandéry et al.[63] demonstrated that only magnetosomes organized in chains instead of individual magnetosomes produce efficient inhibition of cancer cell proliferation. This can be explained by the greater heating efficiency of linearly aligned ferrite NPs when compared to the randomly oriented and agglomerated NPs.[63] The expression, purification, and assembly of our Hcp1_cys3–$CoFe_2O_4$ NPs fibers is less demanding than the purification of magnetosomes from magnetotactic bacteria. This makes the use of the Hcp1_cys3–$CoFe_2O_4$ NPs fibers very promising for MHT studies in the future. Furthermore, our magnetic fibers should be investigated for their theranostics potential, since they combine the properties needed for MRI and MHT. Hence, Hcp1_cys3–$CoFe_2O_4$ NPs fibers could lead to both, increased image contrast and the inhibition of cancer cell proliferation by heating, induced by an alternating magnetic field. The PABNOA approach using the Hcp1_cys3 protein self-assembly with cobalt ferrite nanoparticles, shown here, offers great promise for developing nanocomposite materials with enhanced magnetic properties for use in magnetic data storage or biomedical applications in the future.

4. Experimental Section

Hcp1_cys3 Cloning and Expression: Hcp1Q54C_G91C_N159C (Hcp1_cys3) was used for all experiments. The additional cysteines were introduced at well-oriented and solvent accessible loop regions on the protein rim (Figure S1C,D, Supporting Information). The cloning and expression of Hcp1_cys3 was done according to Schreiber et al.[31] (for details see Methods section in the Supporting Information). The Hcp1 concentration was determined by measuring the absorbance at 280 nm with a NanoDrop ND-1000 from PEQLAB (for details see Data S3 in the Supporting Information).

$CoFe_2O_4$ NP Synthesis: Detailed description of particle synthesis and functionalization are available in the Supporting Information. The cobalt ferrite synthesis was conducted by following the protocol of Cabrera et al.[35] The ligand exchange was conducted according to the modified protocol of Lees et al.[36]

Biohybrid Fiber Assembly: A $CoFe_2O_4$ NP dispersion with a concentration of 0.32×10^{-6} M (based on the mass concentration of 0.12 mg mL^{-1}, mean diameter of 5.5 nm, and density of bulk material of 5.3 g cm^{-3}) was placed in a constant magnetic field of 0.5 T, which was set parallel to the sample. The solution was incubated in the field for 1 h. For sample preparation a constant external magnetic field of 0.5 T was produced by a laboratory electromagnet type B-E10B5 from Bruker. Two equivalents Hcp1_cys3 (0.64×10^{-6} M) based on the NP concentration were added within 1 min to the magnetized NP suspension. After 18 h, a carbon coated TEM grid was aligned parallel to the static magnetic field by hand and dipped into the suspension for 30 min. Finally, the suspension and TEM grid were frozen in liquid nitrogen for 10 min, with the 0.5 T direct magnetic field maintained throughout. The frozen sample was removed and lyophilized under 0.01 mbar vacuum over two days. The reference sample was prepared by the same protocol, but without protein addition step.

Spectroscopic Measurements and TEM/SEM Imaging: The crystal structure of the NP sample was investigated by PXRD Bruker D-8 Advance with CuK-alpha radiation. The X-ray diffraction patterns were collected at 2theta between 10° and 80° over 7 h at room temperature. The IR spectra were recorded using a Perkin-Elmer spectrometer with ATR crystal. The SEM images and EDX analyses were performed utilizing a Hitachi TM 3000 microscope. For the size determination, the length and width of 60 fibers and the size of 60 NP agglomerates were analyzed in the SEM images using ImageJ software.[64] The quantitative EDX analysis was also performed on Hitachi TM 3000 microscope with Bruker EDS Quantax 70 software. For the quantification of the Co:Fe ratio, the analysis of 15 smaller groups of NPs and fiber bundles were performed. For each measurement the Co/Fe atomic ratio was calculated and finally, the standard deviation was calculated. TEM and HRTEM images were collected using a Zeiss Libra120 TEM operated at 120 keV and a JEOL JEM-2200FS microscope operated at 200 keV. For the mean size determination the size of 300 NPs in the TEM image was investigated using ImageJ software.[64] The FFT and HRTEM images were analyzed using Gatan software. The FIB experiment was performed on a Zeiss Neon 40 EsB. An FIB cut with a thickness below 30 nm and a length of 2 µm along the long axis of a fiber was prepared. The cut was stabilized by deposition of a 100 nm thick silicon oxide layer using the ion beam.

The obtained lamellar structure with the nanocomposite in the middle, the silicon substrate on the bottom, and the deposited silicon oxide layer on the top was then transferred to a TEM grid for the TEM and HRTEM investigations.

Magnetic Characterization: The magnetic measurements were accomplished using a SQUID magnetometer, type MPMS XL5 from Quantum Design. The sample was fixed with superglue on a sapphire substrate. The magnetization (M) was recorded at 300 and 2 K at an applied field between 50 000 and –50 000 Oe. ZFC measurements were carried out by cooling the sample from room temperature to 2 K in zero magnetic field, then a static magnetic field of 10 mT was applied. M_{ZFC} was measured during warming up from 2 to 300 K in 1 K steps. The FC measurement was carried out by applying a magnetic field of 10 mT, the M_{FC} was recorded during the subsequent cooling to 2 K in 1 K steps.

Acknowledgements

T.A.P. and A.S. contributed equally to this work. H.C. and S.M.S. conceived the initial project. T.A.P. did most of the experimental work. A.S. did cloning and expression of the proteins used and most of the paper work including the figures. All authors have given approval to the final version of the manuscript. The authors declare no competing financial interest. The authors thank the Baden-Württemberg Foundation—competence network of functional nanostructures (KFN)—(Project B3) for the financial support. A.S. and S.M.S. thank the "Zentrum für Biosystem Analyse" (ZBSA), the Freiburg Institute for Advanced Studies (FRIAS), the Institute for Micro System Engineering (IMTEK) and EXC 294 BIOSS Centre for Biological Signaling Studies, and the Rectorate of the University of Freiburg for support.

Finally, the authors thank Matthias Hagner from University of Konstanz for the FIB cut preparation, Holger Reiner for the HRTEM image, Joe Pearson for the proofreading, as well as Philipp Erler and Nicole Barth for the magnetic measurement.

[1] B. D. Terris, T. Thomson, *J. Phys. D: Appl. Phys.* **2005**, *38*, R199.
[2] B. Balamurugan, D. J. Sellmyer, G. C. Hadjipanayis, R. Skomski, *Scr. Mater.* **2012**, *67*, 542.
[3] K. Hayashi, M. Nakamura, W. Sakamoto, T. Yogo, H. Miki, S. Ozaki, M. Abe, T. Matsumoto, K. Ishimura, *Theranostics* **2013**, *3*, 366.
[4] B. Issa, I. M. Obaidat, B. A. Albiss, Y. Haik, *Int. J. Mol. Sci.* **2013**, *14*, 21266.
[5] M. L. Wegscheid, R. A. Morshed, Y. Cheng, M. S. Lesniak, *Expert Opin. Drug Delivery* **2014**, *11*, 957.
[6] M. H. Oh, J. H. Yu, I. Kim, Y. S. Nam, *ACS Appl. Mater. Interfaces* **2015**, *7*, 22578.
[7] I. Hilger, *Int. J. Hyperthermia* **2013**, *29*, 828.
[8] J. I. Martín, J. Nogués, K. Liu, J. L. Vicent, I. K. Schuller, *J. Magn. Magn. Mater.* **2003**, *256*, 449.
[9] D. Peddis, C. Cannas, A. Musinu, G. Piccaluga, *J. Phys. Chem. C* **2008**, *112*, 5141.
[10] P. Tartaj, T. Gonzalez-Carreno, C. J. Serna, *J. Phys. Chem. B* **2003**, *107*, 20.
[11] A. F. Gross, M. R. Diehl, K. C. Beverly, E. K. Richman, S. H. Tolbert, *J. Phys. Chem. B* **2003**, *107*, 5475.
[12] C. M. Kanamadi, B. K. Das, C. W. Kim, H. G. Cha, E. S. Ji, D. I. Kang, A. P. Jadhav, J. K. Heo, D. Kim, Y. S. Kang, *J. Nanosci. Nanotechnol.* **2009**, *9*, 4942.
[13] N. Frickel, M. Gottlieb, A. M. Schmidt, *Polymer* **2011**, *52*, 1781.
[14] P. Soledad Antonel, G. Jorge, O. E. Perez, A. Butera, A. Gabriela Leyva, R. Martín Negri, *J. Appl. Phys.* **2011**, *110*, 043920.
[15] Q. Dai, D. Berman, K. Virwani, J. Frommer, P. O. Jubert, M. Lam, T. Topuria, W. Imaino, A. Nelson, *Nano Lett.* **2010**, *10*, 3216.
[16] M. Ariyoshi, T. Nishino, H. Iwasaki, H. Shinagawa, K. Morikawa, *Proc. Natl. Acad. Sci. USA* **2000**, *97*, 8257.
[17] M. D. Roy, S. K. Stanley, E. J. Amis, M. L. Becker, *Adv. Mater.* **2008**, *20*, 1830.
[18] N. Kröger, S. Lorenz, E. Brunner, M. Sumper, *Science* **2002**, *298*, 584.
[19] J. L. Arias, M. S. Fernández, *Chem. Rev.* **2008**, *108*, 4475.
[20] R. Blakemore, *Science* **1975**, *190*, 377.
[21] D. Faivre, D. Schüler, *Chem. Rev.* **2008**, *108*, 4875.
[22] S. Abe, M. Tsujimoto, K. Yoneda, M. Ohba, T. Hikage, M. Takano, S. Kitagawa, T. Ueno, *Small* **2012**, *8*, 1314.
[23] T. Douglas, V. T. Stark, *Inorg. Chem.* **2000**, *39*, 1828.
[24] T. Nypelo, C. Rodriguez-Abreu, J. Rivas, M. D. Dickey, O. J. Rojas, *Cellulose* **2014**, *21*, 2557.
[25] S. Galland, R. L. Andersson, V. Strom, R. T. Olsson, L. A. Berglund, *ACS Appl. Mater. Interfaces* **2014**, *6*, 20524.
[26] I. Robinson, L. D. Tung, S. Maenosono, C. Wälti, N. T. K. Thanh, *Nanoscale* **2010**, *2*, 2624.
[27] M. A. Kostiainen, P. Ceci, M. Fornara, P. Hiekkataipale, O. Kasyutich, R. J. M. Nolte, J. J. L. M. Cornelissen, R. D. Desautels, J. van Lierop, *ACS Nano* **2011**, *5*, 6394.
[28] M. A. Kostiainen, P. Hiekkataipale, A. Laiho, V. Lemieux, J. Seitsonen, J. Ruokolainen, P. Ceci, *Nat. Nanotechnol.* **2013**, *8*, 52.
[29] C. Mao, D. J. Solis, B. D. Reiss, S. T. Kottmann, R. Y. Sweeney, A. Hayhurst, G. Georgiou, B. Iverson, A. M. Belcher, *Science* **2004**, *303*, 213.
[30] T. A. Pham, A. Schreiber, E. V. Sturm (née Rosseeva), S. Schiller, H. Cölfen, *Beilstein J. Nanotechnol.* **2016**, *7*, 351.
[31] A. Schreiber, Y. Yuan, M. C. Huber, R. Thomann, A. Ziegler, H. Cölfen, J. Dengjel, M. Krüger, S. M. Schiller, *Adv. Eng. Mater.* **2012**, *14*, B344.
[32] A. Schreiber, M. C. Huber, H. Cölfen, S. M. Schiller, *Nat. Commun.* **2015**, *6*, 6705.
[33] S. M. Bird, J. M. Galloway, A. E. Rawlings, J. P. Bramble, S. S. Staniland, *Nanoscale* **2015**, *7*, 7340.
[34] J. D. Mougous, M. E. Cuff, S. Raunser, A. Shen, M. Zhou, C. A. Gifford, A. L. Goodman, G. Joachimiak, C. L. Ordoñez, S. Lory, T. Walz, A. Joachimiak, J. J. Mekalanos, *Science* **2006**, *312*, 1526.
[35] L. I. Cabrera, A. Somoza, J. F. Marco, C. J. Serna, M. P. Morales, *J. Nanoparticle Res.* **2012**, *14*, 873.
[36] E. E. Lees, T.-L. Nguyen, A. H. A. Clayton, P. Mulvaney, *ACS Nano* **2009**, *3*, 1121.
[37] Cobalt ferrite JCPDS—PDF#221086 [Wavelength = 1.54056].
[38] H. Cohen, A. Gedanken, Z. Zhong, *J. Phys. Chem. C* **2008**, *112*, 15429.
[39] S. P. Schwaminger, P. F. García, G. K. Merck, F. A. Bodensteiner, S. Heissler, S. Günther, S. Berensmeier, *J. Phys. Chem. C* **2015**, *119*, 23032.
[40] Y. Lalatonne, J. Richardi, M. P. Pileni, *Nat. Mater.* **2004**, *3*, 121.
[41] L. Zhang, A. Manthiram, *Phys. Rev. B* **1996**, *54*, 3462.
[42] B. Mehdaoui, R. P. Tan, A. Meffre, J. Carrey, S. Lachaize, B. Chaudret, M. Respaud, *Phys. Rev. B* **2013**, *87*, 174419.

[43] N. Poudyal, B. Altuncevahir, V. Chakka, K. H. Chen, T. D. Black, J. P. Liu, Y. Ding, Z. L. Wang, *J. Phys. D: Appl. Phys.* **2004**, *37*, L45.
[44] V. Blaskov, V. Petkov, V. Rusanov, L. M. Martinez, B. Martinez, J. S. Munoz, M. Mikhov, *J. Magn. Magn. Mater.* **1996**, *162*, 331.
[45] B. D. Cullity, C. D. Graham, *Introduction to Magnetic Materials*, Wiley-IEEE Press, Hobeken, NJ, USA, **2008**.
[46] G. F. Goya, T. S. Berquo, F. C. Fonseca, M. P. Morales, *J. Appl. Phys.* **2003**, *94*, 3520.
[47] D. Caruntu, G. Caruntu, C. J. O'Connor, *J. Phys. D: Appl. Phys.* **2007**, *40*, 5801.
[48] F. Bloch, *Z. Phys.* **1930**, *61*, 206.
[49] L. D. Tung, V. Kolesnichenko, D. Caruntu, N. H. Chou, C. J. O'Connor, L. Spinu, *J. Appl. Phys.* **2003**, *93*, 7486.
[50] J. F. Hochepied, P. Bonville, M. P. Pileni, *J. Phys. Chem. B* **2000**, *104*, 905.
[51] C. Vazquez-Vazquez, M. A. Lopez-Quintela, M. C. Bujan-Nunez, J. Rivas, *J. Nanoparticle Res.* **2011**, *13*, 1663.
[52] G. J. Long, F. Grandjean, in *Proc. NATO Advanced Study Insitute on Supermagnets, Hard Magnetic Materials*, Kluwer Academic Publishers, Boston, MA, USA **1990**.
[53] C. W. Kartikowati, A. Suhendi, R. Zulhijah, T. Ogi, T. Iwaki, K. Okuyama, *Nanoscale* **2016**, *8*, 2648.
[54] Y. Jun, J. Seo, J. Cheon, *Acc. Chem. Res.* **2008**, *41*, 179.
[55] G. Zhen, D. Falconnet, E. Kuennemann, J. Vörös, N. D. Spencer, M. Textor, S. Zürcher, *Adv. Funct. Mater.* **2006**, *16*, 243.
[56] A. Schreiber, E. Zaitseva, Y. Thomann, R. Thomann, J. Dengjel, R. Hanselmann, S. M. Schiller, *Soft Matter* **2011**, *7*, 2875.
[57] C. Altavilla, E. Ciliberto, *Inorganic Nanoparticles: Synthesis, Applications, and Perspectives*, CRC Press, Boca Raton, FL, USA **2011**.
[58] D. Makarov, C. Brombacher, F. Liscio, M. Maret, M. Parlinska, S. Meier, P. Kappenberger, M. Albrecht, *J. Appl. Phys.* **2008**, *103*, 053903.
[59] E. Alphandéry, I. Chebbi, F. Guyot, M. Durand-Dubief, *Int. J. Hyperthermia* **2013**, *29*, 801.
[60] F. Ciardiello, G. Tortora, *N. Engl. J. Med.* **2008**, *358*, 1160.
[61] J. Sudimack, R. J. Lee, *Adv. Drug Delivery Rev.* **2000**, *41*, 147.
[62] E. Alphandéry, S. Faure, O. Seksek, F. Guyot, I. Chebbi, *ACS Nano* **2011**, *5*, 6279.
[63] E. Alphandéry, F. Guyot, I. Chebbi, *Int. J. Pharm.* **2012**, *434*, 444.
[64] C. A. Schneider, W. S. Rasband, K. W. Eliceiri, *Nat. Methods* **2012**, *9*, 671.